On Time-Domain Model-Based Ultrasonic Array Imaging

Fredrik Lingvall and Tomas Olofsson

Abstract—This paper treats time-domain model-based Bayesian image reconstruction for ultrasonic array imaging and, in particular, two reconstruction methods are presented. These two methods are based on a linear model of the array imaging system and they perform compensation in both the spatial and temporal domains using a minimum mean squared error (MMSE) criterion and a maximum a posteriori MAP) estimation approach, respectively. The presented estimators perform compensation for both the electrical and acoustical wave propagation effects for the ultrasonic array system at hand. The estimators also take uncertainties into account, and, by the incorporation of proper prior knowledge, high-contrast superresolution reconstruction results are obtained. The novel nonlinear MAP estimator constrains the scattering amplitudes to be positive, which applies in applications where the scatterers have higher acoustic impedance than the surrounding medium. The linear MMSE and nonlinear MAP estimators are compared to the traditional delay-and-sum (DAS) beamformer with respect to both resolution and signal-to-noise ratio. The algorithms are compared using both simulated and measured data. The results show that the model-based methods can successfully compensate for both sidelobes and grating lobes, and they have a superior temporal and lateral resolution compared to DAS beamforming. The ability of the nonlinear MAP estimator to suppress noise is also superior compared to both the linear MMSE estimator and the DAS beamformer.

I. INTRODUCTION

IN traditional delay-and-sum (DAS) ultrasonic array imaging, the lateral resolution is determined by the physical size of the array and the temporal resolution is determined by the length and shape of the transmit pulse. In more recent array imaging methods [1]–[3], more advanced processing methods have shown that these restrictions can be alleviated resulting in images with both high temporal and lateral resolution, which does not necessarily depend only on the array size and the shape of the transmit pulse. In this article we will discuss time-domain methods to achieve high-resolution imaging results by means of a linear modeling of the array system and a careful choice of reconstruction methods (based on a linear model that acknowledge both uncertainties and prior information regarding the scattering strengths).

Normally in ultrasonic array imaging, an image of the insonified object is formed by (i) transmitting several acoustic pulses which are focused and steered at different parts of the region-of-interest (ROI), or (ii) by means of mechanical scanning using a wide-beam transducer and then constructing an image from the collected RF-data. The first method will be denoted physical array imaging (PAI) in this article and the latter synthetic array imaging (SAI).

Traditionally, acoustic array data, both from physical and synthetic arrays, have been processed by means of spatial filtering, or beamforming, to obtain an image of the scattering objects [4], [5]. Beamforming, using the classical time-domain DAS method, is analogous to the operation of an acoustical lens, and it can be performed efficiently using delay-line operations in real time or using postprocessing as in SAI systems [6]–[8]. Conventional beamforming, which is essentially based on a geometrical optics approach [9], is computationally attractive due to its simplicity but it has several inherent drawbacks. In particular, conventional beamforming does not perform well using sparse arrays or using arrays where the element size is large compared to the wavelength of the transmitted waveform.[1]

In this paper we will consider more advanced models of the imaging system which then will be used in the image reconstruction process. The approach taken here is Bayesian-influenced, and we view the array imaging problem as an inference problem. We will show that the three factors below are important for the reconstruction performance:

- The use of prior information regarding scattering strengths is vital to obtain stable estimates.
- We must consider the uncertainties (model errors and measurement noise) that we have.
- A suitable model for the imaging system is important in order to be able to compensate for diffraction effects and the electrical characteristics of the array system.

By acknowledging these three factors we can obtain very high resolution images, even though our imaging system may not be perfect in the sense of traditional array imaging (i.e., well-sampled arrays with small array elements).

The main motivation for developing the reconstruction algorithms discussed here is the wish to improve the per-

F. Lingvall is with the Department of Informatics, Group for Digital Signal Processing and Image Analysis, University of Oslo, NO-0316 Oslo, Norway (e-mail: Fredrik.Lingvall@ifi.uio.no).

T. Olofsson is with the Signals and Systems Group, Department of Engineering Sciences, Uppsala University, SE-751 20 Uppsala, Sweden.

[1]Grating lobes, which occur for sparse or under-sampled arrays, is, in fact, a direct consequence of DAS processing [10].

formance of traditional ultrasonic array imaging methods. In particular, it is desirable to relax the restrictions of the array design imposed by the DAS method, that is, the requirement of an array pitch less than half the transmitted wavelength and the need to use small array elements so that the point source assumption is valid. Moreover, in many applications a high frame rate is desirable and the limiting factor is often the round-trip travel time of the acoustic pulse. If many points could be reconstructed from a single transmission, then the frame rate could be increased significantly. Such systems have been proposed before where a wider-than-normal transmit beam is used and a few lines of the total ROI are reconstructed using a parallel receive beamformer [11]–[13]. These systems can, however, beamform only a few lines per transmission. The methods proposed here do not have these restrictions and their performance depends, as will be shown later, mainly on the signal-to-noise ratio (SNR).

In this article we will see that, by using a suitable model for the imaging system and appropriate assumptions on the scattering amplitudes, the reconstruction performance can be significantly improved compared to traditional DAS imaging.

This article is organized as follows: In Section II the linear model is introduced, and the reconstruction methods based on the model is described in Section III. The simulations and experiments are given in Sections IV and V, respectively, and the conclusions are finally given in Section VI.

II. The Impulse Response Model

In order to compensate for the frequency-dependent diffraction effects, input pulse shape, and the electro-acoustical properties of the array system, we need a model that is more advanced than the common point-source model. We have chosen a linear model here which is sufficient for our purposes. It has been shown to be adequate for compensating transducer size effects in SAI [14] as well as to compensate for grating lobes in undersampled linear arrays [15]. Note that we do not consider the model used here to be flawless but it is sufficient for our purposes; that is, it allows us to compensate for many of the effects that cause problems in traditional DAS imaging.

The linear model used here is based on the impulse response method [14], [16]–[19], where each observation point is associated with an impulse response. The impulse response can be divided into the forward (f), or transmit, impulse response and the backward (b), or receive, impulse response. We make a distinction between the forward and backward impulse responses since the transmit and receive apertures may not be identical, and the electrical characteristics of the transmitters and receivers may also differ.

The forward response can be divided into three parts: the input signal $u(t)$, the forward electro-acoustical response $h^{\text{ef}}(t)$, and the forward acoustical or spatial impulse response (SIR) $h^{\text{f-SIR}}(\mathbf{r}, t)$. In the simulations performed in
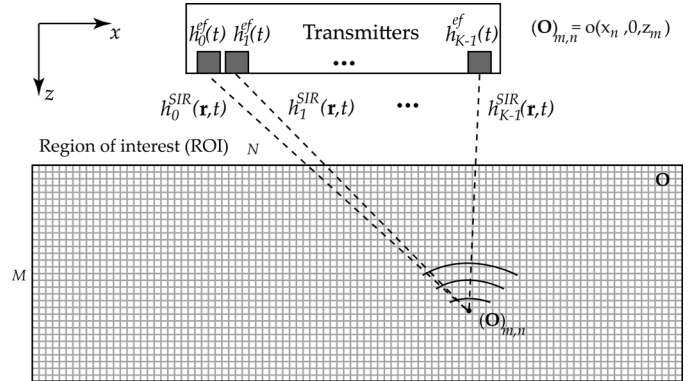

Fig. 1. Illustration of the transmit process for a single observation point at $\mathbf{r} = (x_n, 0, z_m)$ in the x–z plane.

this article, the input signals are of the form $\delta(t - \tau)$ where τ is the focusing delay for the corresponding transmit element. The model described below is, however, not limited to this type of input signals; that is, any type of input pulse can be used in the model.

The SIRs account for the acoustical diffraction effects associated with the transmit elements and they can be obtained by several means such as analytic solutions to the wave equation, numerical procedures [20], [21], or measurements.[2] The transmit process for a single observation point in the x–z plane is illustrated in Fig. 1. Note that the total forward impulse response is a superposition of the forward impulse responses corresponding to all transmit elements.

The backward response can be similarly divided into two parts, the backward acousto-electrical impulse response $h^{\text{eb}}(t)$ and the backward SIR $h^{\text{b-SIR}}(\mathbf{r}, t)$.

Now, consider an array with K transmit elements and L receive elements and contributions from a single observation point, $\mathbf{r} = \begin{bmatrix} x & y & z \end{bmatrix}^T$, where ^{T} denotes the transpose operator. The received signal, $y_l(\mathbf{r}, t)$, from the lth receive element can be expressed

$$
y_l(\mathbf{r},t) = \left(\overbrace{\sum_{k=0}^{K-1} h_k^{\text{f-SIR}}(\mathbf{r},t) * h_k^{\text{ef}}(t), * u_k(t)}^{\text{Forward impulse response (f)}} \right) o(\mathbf{r}) *
$$
$$
\overbrace{h_l^{\text{b-SIR}}(\mathbf{r},t) * h_l^{\text{eb}}(t)}^{\text{Backward impulse response (b)}} + e_l(t),
$$
$$
= h^{\text{f}}(\mathbf{r},t) * h_l^{\text{b}}(\mathbf{r},t) o(\mathbf{r}) + e_l(t),
$$
$$
= h_l(\mathbf{r},t) o(\mathbf{r}) + e_l(t),
$$

(1)

where $*$ denotes temporal convolution, and $e_l(t)$ is the noise for the lth receive element. The object function $o(\mathbf{r})$ is the scattering strength at $\mathbf{r}$, $h_k^{\text{ef}}(t)$ is the forward electrical impulse response for the kth transmit element, $h_l^{\text{eb}}(t)$ is the backward electrical impulse response for the lth receive element, and $u_k(t)$ is the input signal for the kth transmit element. Hereafter we will refer to the pulse-echo (double-path) impulse $h_l(\mathbf{r}, t)$ as the system impulse response.

A discrete-time version of (1) is obtained by sampling the impulse responses and by using discrete-time convolutions. If we, for simplicity, consider two-dimensional (2-D) imaging, where the scatterers are located in the x–z plane (cf. Fig. 1), then the received discrete waveform from a target at an observation point $\mathbf{r} = (x_n, 0, z_m)$ can be expressed as

$$\mathbf{y}_l^{(m,n)} = \mathbf{h}_l^{(m,n)}(\mathbf{O})_{m,n} + \mathbf{e}_l, \tag{2}$$

where the column vector $\mathbf{h}_l^{(m,n)}$ is the discrete system impulse response for the lth receive element, and $\mathbf{e}_l$ is the noise vector for the lth receive element.[3] The $M \times N$ matrix $\mathbf{O}$ represents the scattering amplitudes in the ROI, and the notation $(\mathbf{O})_{m,n}$ denotes element (m,n) in $\mathbf{O}$.

To obtain the received signal for all observation points, we need to perform a summation over m and n, which equivalently can be expressed as a matrix-vector multiplication,

$$
\begin{aligned}
\mathbf{y}_l &= \sum_{m,n} \mathbf{h}_l^{(m,n)}(\mathbf{O})_{m,n} + \mathbf{e}_l, \\
&= \left[\mathbf{h}_l^{(0,0)} \ \mathbf{h}_l^{(1,0)} \ \cdots \ \mathbf{h}_l^{(M-1,N-1)} \right] \mathbf{o} + \mathbf{e}_l, \\
&= \mathbf{P}_l \mathbf{o} + \mathbf{e}_l,
\end{aligned} \tag{3}
$$

where the vector $\mathbf{o}$ is the vectorized matrix $\mathbf{O}$ [$\mathbf{o} = \text{vec}(\mathbf{O})$].

If we now append all L receive signals $\mathbf{y}_l$ into a vector $\mathbf{y}$, then we finally obtain the linear model

$$
\mathbf{y} = \begin{bmatrix} \mathbf{y}_0 \\ \mathbf{y}_1 \\ \vdots \\ \mathbf{y}_{L-1} \end{bmatrix} = \begin{bmatrix} \mathbf{P}_0 \\ \mathbf{P}_1 \\ \vdots \\ \mathbf{P}_{L-1} \end{bmatrix} \mathbf{o} + \begin{bmatrix} \mathbf{e}_0 \\ \mathbf{e}_1 \\ \vdots \\ \mathbf{e}_{L-1} \end{bmatrix},
$$
$$
= \mathbf{P}\mathbf{o} + \mathbf{e}, \tag{4}
$$

for the total array imaging system [15]. The propagation matrix, $\mathbf{P}$, in (4) now describes both the transmission and the reception process for an arbitrary focused array.[4] Note that

- each column in $\mathbf{P}$ is the vectorized B-scan response for a unit area point target at the corresponding observation point. The received vectorized B-scan data $\mathbf{y}$ is thus a weighted sum of B-scan responses for all observation points.
- the "noise" vector $\mathbf{e}$ describes the uncertainty of the model (4). Hence, $\mathbf{e}$ not only models the measurement noise but also all other errors that we may have, such as multiple scattering effects, cross talk between array elements, nonuniform sound speed in the media, etc.

[3]All vectors are, by convention, column vectors in this article.
[4]We have chosen to derive the linear model (4) using a 1-D linear array and a 2-D rectangular sampling grid of the ROI. This was done only in order to simplify the presentation. The array elements can, in fact, be positioned at arbitrary locations in 3-D space, and the observation points do not need to be confined to a regularly sampled grid in 2-D space. Thus, the model (4) can also be used to model 2-D arrays as well as array responses in 3-D space.

The model (4) plays a vital part of the image reconstruction methods discussed in this paper. The model (4) allows us to compensate for many properties such as sidelobes, grating lobes, and the electrical characteristics of the array system. In Section III below, the model (4) will be utilized, and two reconstruction methods based on the model will be presented.

III. BAYESIAN IMAGE RECONSTRUCTION METHODS

In Bayesian estimation theory a probability density function (PDF) describes the uncertainty, or the degree of belief, of the true value of the variable under study [23]. In other words, a PDF is thought of as a carrier of information. In our case we want to study the scattering strength at each image point described by the vector $\mathbf{o}$. To accomplish this we perform an experiment that gives us some data $\mathbf{y}$. Note that our knowledge regarding $\mathbf{o}$ is usually not coming only from the data. Typically we know, without seeing any data, that $\mathbf{o}$ cannot have an arbitrary scattering amplitude; the scattering amplitude must at least be limited to some interval. The PDF $p(\mathbf{o}|I)$, that describes our knowledge before seeing the data, is usually called "the prior", and I denotes any background information that we have regarding $\mathbf{o}$. When we have performed an experiment, we have received more information about $\mathbf{o}$ and the updated PDF after seeing the data are given by the posterior PDF, $p(\mathbf{o}|\mathbf{y}, I)$. If the measurement contained relevant (new) information of $\mathbf{o}$, then the posterior PDF should be more concentrated around the true value of $\mathbf{o}$.

Bayes' theorem,

$$p(\mathbf{o}|\mathbf{y}, I) = p(\mathbf{o}|I)\frac{p(\mathbf{y}|\mathbf{o}, I)}{p(\mathbf{y}|I)}, \tag{5}$$

describes how to update our knowledge of the variable, $\mathbf{o}$, when new data, $\mathbf{y}$, are observed. The conditional PDF $p(\mathbf{y}|I)$ is a normalization factor not dependent on $\mathbf{o}$, and $p(\mathbf{y}|\mathbf{o}, I)$ describes the likelihood of seeing the data $\mathbf{y}$, given $\mathbf{o}$.

In this paper the errors $\mathbf{e}$ are assumed to be Gaussian, and $p(\mathbf{y}|\mathbf{o}, I)$ will therefore be given by the multidimensional Gaussian distribution,

$$p(\mathbf{y}|\mathbf{o}, I) = \frac{1}{(2\pi)^{\frac{MN}{2}}|\mathbf{C}_\mathrm{e}|^{1/2}} e^{-\frac{1}{2}(\mathbf{y}-\mathbf{P}\mathbf{o})^T \mathbf{C}_\mathrm{e}^{-1}(\mathbf{y}-\mathbf{P}\mathbf{o})}, \tag{6}$$

where $\mathbf{P}$ is the propagation matrix from (4), $\mathbf{C}_\mathrm{e}$ is the covariance matrix $\mathbf{C}_\mathrm{e} = \mathrm{E}\{\mathbf{e}\mathbf{e}^T\}$, and $\mathrm{E}\{\cdot\}$ is the expectation operator.

The two most common estimators in Bayesian estimation applications are the maximum *a posteriori* (MAP) estimator and the minimum mean square error (MMSE) estimators. The MAP estimate is defined as the maximizing argument of $p(\mathbf{o}|\mathbf{y}, I)$,

$$\hat{\mathbf{o}}_{\mathrm{MAP}} = \arg\max_{\mathbf{o}} p(\mathbf{o}|\mathbf{y}, I) = \arg\max_{\mathbf{o}} p(\mathbf{o}|I)p(\mathbf{y}|\mathbf{o}, I), \tag{7}$$
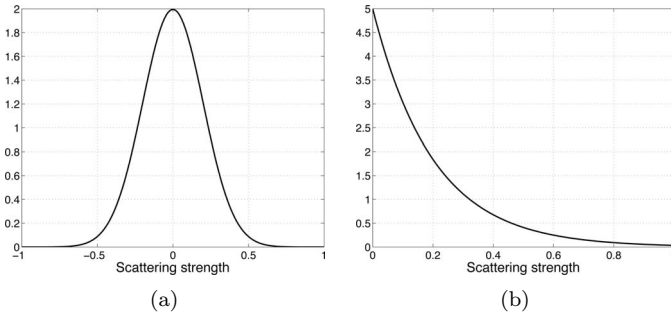
Fig. 2. Illustration of the *a priori* probability density functions (PDF) used for the scattering strengths $(\mathbf{O})_{m,n}$ in this article. (a) The 1-D Gaussian PDF. (b) The 1-D exponential PDF.

where (5) was used in the last equality. The MAP estimate is thus the value **o** that is most probable, given both data and prior information.

The MMSE estimate is defined by

$$\hat{\mathbf{o}}_{\mathrm{MMSE}} = \arg\min_{\mathbf{o}} \mathrm{E}\{\|\mathbf{o} - \hat{\mathbf{o}}\|^2\}. \tag{8}$$

In this paper we focus on two estimators for estimating the scattering strengths. They are based on two different assumptions:

1. Both **o** and **e** are zero-mean Gaussian processes.
2. The scattering amplitudes **o** are positive and exponentially distributed, and **e** is zero-mean Gaussian.

To see more clearly what these *a priori* assumptions mean, consider the 1-D Gaussian and the exponential PDFs shown in Fig. 2. We see here that small amplitudes are more likely than large ones, and the width (the variance) of the PDFs tells us how large are variations in the scattering strengths that we expect. Roughly, we assume here that only the scattering energy must be limited (it is very unlikely to have very large scattering amplitudes). This is actually a rather conservative assumption since we know that the scattering amplitudes must in reality be limited to some fixed interval.[5] Furthermore, these prior assumptions are also attractive since they, as will be discussed below, lead to relatively efficient algorithms.

In practice, the mean and variance values may not be known exactly. In such case one can, more practically, see mean and variance values simply as tuning parameters for the algorithms. The authors' experience is also that the reconstruction performance is not too sensitive regarding

[5]The *a priori* distributions used here can also be motivated from an information theoretic perspective. Say that we have knowledge of the expected scattering variance (energy) of **o** and that we have no reason to favor positive amplitudes over negative ones, so the mean must be zero. What prior should we then assign to **o**? Clearly, we do not want that our choice of prior should add more information about **o** than we have. Thus, we want the prior to be absolutely noncommittal for everything except for the information that actually we have. It turns out that the Gaussian PDF is the most noncommittal PDF if the mean and variance are known, and the exponential PDF is the most noncommittal PDF if we know the mean and that **o** is positive; the most noncommittal distribution is the one that has the maximum entropy, given the prior information. We recommend [23] for more information regarding this subject.

the exact value of these parameters, as will be discussed further in Section IV-D.

A. The Linear MMSE Estimator

The optimal linear estimator, which has the form $\hat{\mathbf{o}} = \mathbf{K}\mathbf{y}$, is based on the assumptions that both **o** and **e** are Gaussian distributed and the estimator is found minimizing a mean squared error criterion,

$$\begin{aligned}
\mathbf{K}_{\mathrm{LMMSE}} &= \arg\min_{\mathbf{K}} \mathrm{E}\{\|\mathbf{o} - \mathbf{K}\mathbf{y}\|^2\} \\
&= \arg\min_{\mathbf{K}} \mathrm{tr}\{\mathbf{C}_{\mathrm{o}}\} - 2\mathrm{tr}\{\mathbf{K}^T\mathbf{C}_{\mathrm{o}}\mathbf{P}^T\} \\
&\quad + \mathrm{tr}\{\mathbf{K}\mathbf{P}\mathbf{C}_{\mathrm{o}}\mathbf{P}^T\mathbf{K}^T\} + \mathrm{tr}\{\mathbf{K}\mathbf{C}_{\mathrm{e}}\mathbf{K}^T\},
\end{aligned} \tag{9}$$

where $\mathbf{y} = \mathbf{P}\mathbf{o} + \mathbf{e}$ and where we assume that **o** and **e** are mutually independent with covariance matrices $\mathbf{C}_{\mathrm{o}} = \mathrm{E}\{\mathbf{o}\mathbf{o}^T\}$ and $\mathbf{C}_{\mathrm{e}} = \mathrm{E}\{\mathbf{e}\mathbf{e}^T\}$, respectively. The linear MMSE (LMMSE) estimator, $\hat{\mathbf{o}} = \mathbf{K}_{\mathrm{LMMSE}}\mathbf{y}$, is presented here for reasons of comparison since it is closely related to the novel MAP estimator presented in Section III-B. The LMMSE estimator is given by [3], [15]

$$\mathbf{K}_{\mathrm{LMMSE}} = \mathbf{C}_{\mathrm{o}}\mathbf{P}^T(\mathbf{P}\mathbf{C}_{\mathrm{o}}\mathbf{P}^T + \mathbf{C}_{\mathrm{e}})^{-1}. \tag{10}$$

Furthermore, by also assuming that the covariance matrices $\mathbf{C}_{\mathrm{o}}$ and $\mathbf{C}_{\mathrm{e}}$ have the form $\mathbf{C}_{\mathrm{o}} = \sigma_{\mathrm{o}}^2\mathbf{I}$ and $\mathbf{C}_{\mathrm{e}} = \sigma_{\mathrm{e}}^2\mathbf{I}$, (10) reduces to

$$\mathbf{K}_{\mathrm{LMMSE}} = \mathbf{P}^T(\mathbf{P}\mathbf{P}^T + \mu\mathbf{I})^{-1}, \tag{11}$$

where $\mu = \sigma_{\mathrm{e}}^2/\sigma_{\mathrm{o}}^2$. The optimal linear estimator (11) has been shown to be able to successfully compensate for finite-sized array elements in SAI [14] as well as to suppress sidelobes and grating lobes in PAI [15].

B. The MAP Estimator for Positivity-Constrained Scattering

In Section III-A it was assumed that **o** could take both negative and positive values. Such an assumption is reasonable if the inspected object may have an acoustic impedance that can be both higher and lower from that of the surrounding medium. In some applications it may, however, be appropriate to assume that the scattering strength only can take positive values.[6] Such applications can be found in, for example, nondestructive testing, sonar mapping, sea-floor imaging, etc. Let us therefore consider a scenario where it is known *a priori* that the scatterers have a higher acoustic impedance than the surrounding medium (resulting in positive scattering amplitudes). Also, let us assume that **o**, instead of being Gaussian, has elements that are exponentially distributed, thus allowing only for positive values. If we also assume that all o_is are independent identically distributed (IID), then the prior is given by

$$p(\mathbf{o}|I) = \Pi_{i=0}^{MN-1}\lambda_{\mathrm{o}}\exp(-\lambda_{\mathrm{o}}o_i). \tag{12}$$

[6]This method can also be derived for scattering that is strictly negative using the negative single-sided exponential distribution.

Using that $\mathbf{e}$ is Gaussian results in the posterior PDF

$$
\begin{aligned}
p(\mathbf{o}|\mathbf{y}, I) \propto & \frac{1}{(2\pi)^{\frac{MN}{2}}|\mathbf{C}_e|^{1/2}} \\
& \exp\left(-\frac{1}{2}(\mathbf{y} - \mathbf{Po})^T \mathbf{C}_e^{-1}(\mathbf{y} - \mathbf{Po})\right) \\
& \Pi_{i=0}^{MN-1} \lambda_o \exp(-\lambda_o o_i).
\end{aligned} \quad (13)
$$

The MAP estimate can be found by finding the argument minimizing the negative log of (13). Thus, the MAP estimate can then be found by solving the quadratic programming (QP) problem

$$
\begin{aligned}
\hat{\mathbf{o}} = & \arg\min_{\mathbf{o}} \frac{1}{2}(\mathbf{y} - \mathbf{Po})^T \mathbf{C}_e^{-1}(\mathbf{y} - \mathbf{Po}) + \lambda_o \mathbf{1}^T \mathbf{o} \\
& \text{subject to} \quad o_i \geq 0 \; \forall i,
\end{aligned} \quad (14)
$$

where $\mathbf{1} = [1\ 1\ \cdots\ 1]^T$. The estimate obtained by solving (14) will hereafter be denoted the positivity constrained quadratic programming, or PCQP, estimate.

QP problems can always be solved in a finite number of iterations, if a solution exists [24]. Here, the QP problem is convex since the Hessian matrix, $\mathbf{P}^T \mathbf{C}_e^{-1} \mathbf{P}$, is positive semidefinite which further facilitates the solution of the problem.

IV. SIMULATIONS

In this section we will study, by means of simulations, the behavior of the proposed LMMSE and PCQP estimators. The simulated data used here were obtained using the linear model (4), where the noise vector $\mathbf{e}$ was simulated as white with Gaussian amplitude distribution. In all simulations performed here, a certain amount of noise has been used since a noise-free measurement situation is unrealistic.[7] The SNR used in this article is defined as

$$
\gamma \triangleq \frac{\mathbf{o}^T \mathbf{P}^T \mathbf{Po}}{\mathbf{e}^T \mathbf{e}}. \quad (15)
$$

The signal energy, $\mathbf{o}^T \mathbf{P}^T \mathbf{Po}$, is then the total (noise-free) energy received by all array elements.[8] Note that the received signal energy when, for example, imaging a single point target will depend on the target's position. The SNR will therefore also be a function of the target's position and, consequently, the SNR will be low when the target is in regions with low acoustic energy and high when the target is in the main lobe (or in a grating lobe).

In Section IV-A–C below, we will study the proposed model-based methods with respect to three important factors: imaging with finite-sized array elements, imaging with undersampled arrays, and the influence of SNR for

[7]The estimates of the LMMSE and PCQP estimators would essentially be error free in such a case.

[8]The noise-free signal energy is found by setting $\mathbf{e} = 0$ in (4), that is, $\mathbf{o}^T \mathbf{P}^T \mathbf{Po} = \mathbf{y}^T \mathbf{y}|_{\mathbf{e}=0}$.
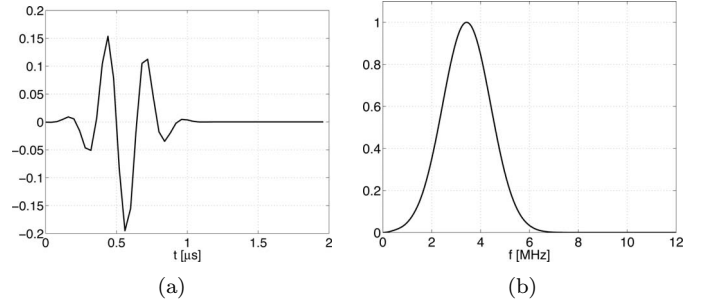

Fig. 3. The electrical impulse response used in the simulations. (a) Simulated electrical impulse response. (b) Amplitude spectrum.

the reconstruction performance, respectively. The estimators will also be compared with traditional DAS beamforming.

In all simulations in this article, the forward and backward electrical impulse responses have a corresponding center frequency of 3.5 MHz, as shown in Fig. 3. The wavelength, λ, at the center frequency is then 0.43 mm for a sound speed of 1500 m/s.

A. Imaging with Finite-Sized Array Elements

Imaging with a finite-sized aperture, that is, using a transmitter where the size is in the same order (or larger) than the wavelength of the acoustic pulse, is common in many applications. In such imaging, the specific diffraction effects due to the finite aperture cannot be neglected. These effects are most significant close to the aperture, and the LMMSE and PCQP methods are here studied for a such case. A 32-element array, focused at $z = 25$ mm, with a 0.5-mm pitch and 5×10-mm elements, has been used. Such an array is not realizable in PAI, since the elements are larger than the array pitch, but it can be used in SAI.

In Fig. 4(a), a snapshot of the wave field at ($x = -25$–25 mm, $z = 15$–25 mm) is shown. It is apparent that the wave field differed significantly from that of a focused array with point-like elements since the field at the focal point roughly has the same width as the array elements.

The reconstruction results, shown in Fig. 4(b)–(d), are computed for a unit area point target located at the focal point ($x = 0$ mm, $z = 25$ mm). As can be seen in the DAS-processed image, shown in Fig. 4(b), the DAS beamforming has resulted in a lateral resolution that is in the same order as the size of the transmitters. The model-based LMMSE and PCQP methods, on the other hand, have both successfully compensated for the size effects of the array elements, as can be seen in Fig. 4(c) and (d).

B. Imaging with Undersampled Arrays

Imaging with undersampled, or sparse arrays, is attractive since this allows for larger array elements in PAI due to a larger array pitch, and the hardware complexity of the array system is decreased compared to that of a dense array [25]. This is of particular interest for 2-D arrays where
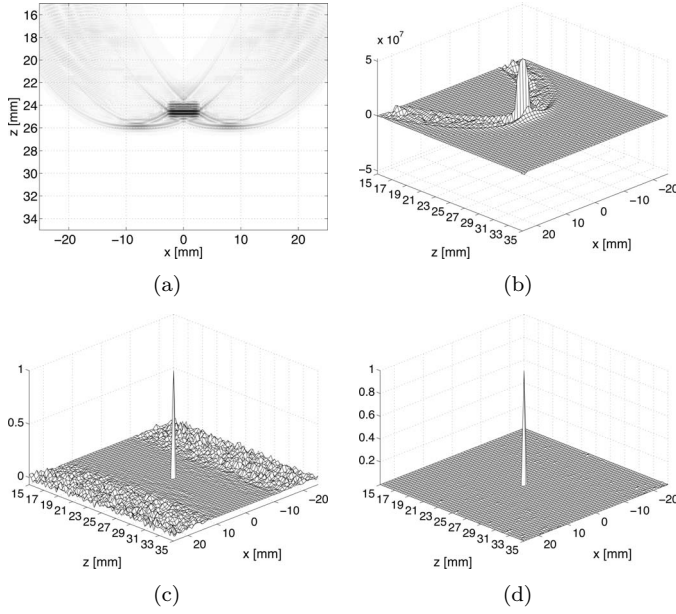
Fig. 4. Wave field snapshot (a) and reconstruction images (b), (c), and (d) using the DAS, LMMSE, and PCQP algorithms, respectively, for a 32-element array with, pitch = 0.5 mm (5 × 10 mm elements, and a unit amplitude point target at $x = 0$ mm) at $z = 25$ (SNR = 21.3 dB). (a) Simulated snapshot of the acoustic field at -25 mm $< x < 25$ mm, 15 mm $< z < 35$ mm. (b) DAS. (c) LMMSE. (d) PCQP.
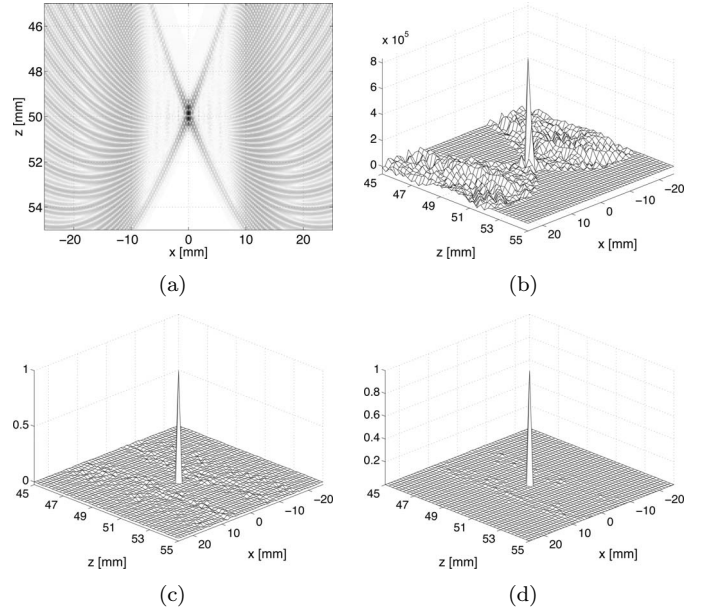

Fig. 5. Wave field snapshot (a) and reconstruction images (b), (c), and (d) using the DAS, LMMSE, and PCQP algorithms, respectively, for an undersampled 32-element array with, pitch $= 2$ mm (5×10 mm elements, and a unit amplitude point target at $x = 0$ mm) agt $z = 25$ (SNR = 11.9 dB). (a) Simulated snapshot of the acoustic field at -25 mm $< x < 25$ mm, 45 mm $< z < 55$ mm. (b) DAS. (c) LMMSE. (d) PCQP.

the number of, for example, connectors rapidly becomes large for dense arrays [26].

In traditional DAS array imaging, one must carefully consider the position of the array elements and the aperture weighting since, otherwise, sidelobes and grating lobes can deteriorate the contrast in the image. The model-based methods proposed here have the ability to compensate for essentially any beam pattern; hence a more flexible array design should be possible. To illustrate this property, a simulation with a 32-element undersampled array is shown in Fig. 5. The array has a pitch of 2 mm which is roughly 4λ (at the center frequency of the pulse). Fig. 5(a) shows a simulated snapshot of the transmitted waveform, and it can be seen that there are strong grating lobes for $x \gtrsim \pm 10$ mm.

The simulated data were obtained using a unit area point source at the focal point ($x = 0$ mm, $z = 50$ mm). The DAS beamformed result is shown in Fig. 5(b), and it is evident that the grating and sidelobes result in a substantial leakage. As can be seen in Fig. 5(c) and (d), the model-based LMMSE and PCQP methods both successfully compensated for these effects, and the leakage, for both of the model-based methods, is minimal.

C. Performance with Respect to SNR

In this section the PCQP estimator is compared with the DAS beamformer and the LMMSE estimator for a fixed setup but with a varying SNR. The objective is to show the importance of prior information regarding the scattering strengths for obtaining good estimates. As de-
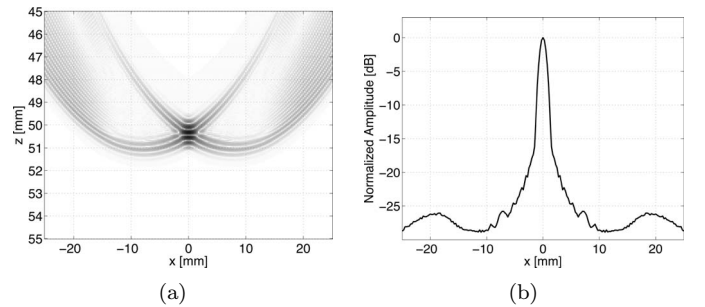

Fig. 6. Snapshot of the acoustic field at -25 mm $< x < 25$ mm, 45 mm $< z < 55$ mm for a 16-element linear array with 0.9-mm-wide elements, and an array pitch of 1 mm focused at $z = 50$ mm. (a) Wave field snapshot at $t = 34.6$ μs. (b) Profile plot of the wave field.

scribed in Section III-B, the prior for the PCQP method is based on positivity constraints on the scattering amplitudes and it will be shown below that such knowledge can greatly improve the reconstruction performance.

Here, the simulations are performance using a 16-element array with pitch 1 mm, and 0.9×10-mm elements, focused at $z = 50$ mm. A snapshot of the acoustic field around the focal point for this setup is shown in Fig. 6. Since the array is undersampled, one can notice two grating lobes, at approximately $x = \pm 18$ mm, but most of the acoustic energy is focused around the center axis $x = 0$.

Three simulations were performed, with SNR = 18, 3.4, and -10.1 dB, where the SNR is defined by (15). The true scattering image, $\mathbf{o}$, had five pairs of unit area point targets located at the horizontal positions $x = -20, -10, 0, 10,$

and 20 mm, and vertically at $z = 50$ and $z = 50.5$ mm. The vertical distance between the point targets is then roughly one wavelength at the corresponding center frequency of the array.

To obtain a fair comparison, we need to set the parameters in the LMMSE and the PCQP so that the expected energy using both estimators is the same. The prior that is determined by the mean value λ_o, used in the PCQP estimator, was based on the assumption that we can expect to find one unit area point target in the ROI. The mean scattered energy is the sum of the squared mean value and the variance, which for a single point target becomes $1^2/MN = \lambda_o^2 + \lambda_o^2$, since the variance is given by λ_o^2 for the exponential PDF. Thus, λ_o is given by $1/\sqrt{2MN}$. By similar reasoning, the variance, σ_o^2, used in the LMMSE estimator is given by $\sigma_o^2 = 1/MN$.

The reconstruction results, for the respective SNRs, are displayed in Fig. 7. If we study the DAS beamformed images, it is evident that, even for the data with the relatively high SNR of 18 dB, shown in Fig. 7(b), the DAS method can only resolve the targets located close to the focal point. On the contrary, the LMMSE and PCQP estimators were able to resolve all targets. The PCQP estimator had, as it can be seen in Fig. 7(d), very low error in the scattering amplitudes at all target positions.

When decreasing the SNR to 3.4 dB, the LMMSE and the PCQP estimators underestimated the amplitudes in the regions where the acoustic power was low, shown in Fig. 7(g) and (h), which is a reasonable behavior since the SNR in those regions is lower than in the focusing region, and the estimates are therefore more uncertain; that is, the estimators become more cautious at regions with low acoustic power. This is even more evident in the reconstructions from the rather low SNR of -10.1 dB, shown in Fig. 7(j)–(l). Now, the LMMSE and PCQP estimators only trust responses from the focusing region, and all other responses are close to zero.

Noteworthy in Fig. 7(h) and (l) is also the remarkable high ability of the PCQP estimator to suppress the noise, even though the received signals were completely hidden in the noise; see Fig. 7(i). The PCQP estimator managed to predict the two targets at the focal point with a remarkable high contrast in the reconstructed image.

It is evident from these simulations that the two model-based LMMSE and PCQP methods are superior to traditional DAS-based beamforming, DAS processing does not perform well for targets outside the focusing region, whereas the two model-based LMMSE and PCQP methods can reconstruct the targets with high temporal and lateral resolution provided that the SNR is sufficiently high.

D. Sensitivity to the SNR Setting

In practice, the SNR is normally not known exactly. The statistics of the measurement noise may be obtained from measurements but other uncertainties included in $\mathbf{e}$, such as model errors and nonlinear effects, is difficult to measure. Typically, one can then treat the SNR setting

for the LMMSE and PCQP estimators as tuning parameters. An important question is then: how sensitive are these algorithms for variations in this parameter? To answer this question we illustrate the behavior of the model-based methods (when the SNR setting deviates from the true value) by presenting simulated reconstruction results with the same setup as used in Section IV-C. We present reconstruction results for four different SNR settings in Fig. 7. In Fig. 8(a) and (c), the SNR settings were 4 times too low compared to the true value. By comparing with the reconstruction results when using the true SNR value, shown in Fig. 7(g) and (h), respectively, one can see that both estimators have become more conservative and underestimated the amplitudes of scatterers outside the focal zone. If we instead use a 4-times-too-high SNR setting, shown in Fig. 8(b) and (d), the estimated amplitude of the scatterers is closer to the true value but at the cost of more noisy reconstructions. This trend is seen even more clearly in Fig. 8(e)–(h) where the deviations from the true values were ± 10 times. Note that even though the deviations from the true SNR values were as large as 10 times, none of the methods became unstable (with possibly useless results as a consequence).

The simulation results presented here are in agreement with the well-known properties of Bayesian estimators; that is,

- If the noise is large, then we have more trust in the prior than in the data.
- If the noise is low, then the prior is not so important and we rely mostly on the data.

These properties can be seen in the LMMSE estimator (10) by considering the two extreme cases when the noise increases to infinity and decreases to 0. Let us first consider when the noise is large. If the noise increases, then the matrix $\mathbf{C}_e$ will be dominating in the factor $(\mathbf{P}\mathbf{C}_o\mathbf{P}^T + \mathbf{C}_e)$ and (10) reduces to

$$\hat{\mathbf{o}} = \mathbf{K}_{\text{LMMSE}}\mathbf{y} \approx \mathbf{C}_o\mathbf{P}^T\mathbf{C}_e^{-1}\mathbf{y}$$
$$= \sigma_o^2 \frac{\mathbf{P}^T\mathbf{y}}{\sigma_e^2}, \tag{16}$$

where we have used (11) in the last equality. Thus the LMMSE estimator reduces to a matched filter, $\mathbf{P}^T\mathbf{y}$, when the noise is large (which has the well-known property to optimize the SNR at a single point).[9] If the noise approaches infinity $\sigma_e^2 \rightarrow \infty$, then $\hat{\mathbf{o}} \rightarrow \mathbf{0}$; that is, $\hat{\mathbf{o}}$ approaches the *a priori* mean value.

If we now consider the other extreme case, when we have a very high SNR, then $\mathbf{P}\mathbf{C}_o\mathbf{P}^T$ will dominate the factor $(\mathbf{P}\mathbf{C}_o\mathbf{P}^T + \mathbf{C}_e)$ and the LMMSE estimator reduces to:

[9]Note that a matched filter only optimizes the SNR at a single point without considering surrounding observation points. A matched filter has, in fact, similarities to the conventional DAS beamformer which can be expressed in the matrix form $\mathbf{D}^T\mathbf{y}$ where the sparse matrix $\mathbf{D}$ only has ones at those positions corresponding to focusing delays [14]. The matched filter will, therefore, also have many of the deficiencies that the DAS beamformer has, such as problems with grating lobes, sidelobes, etc.
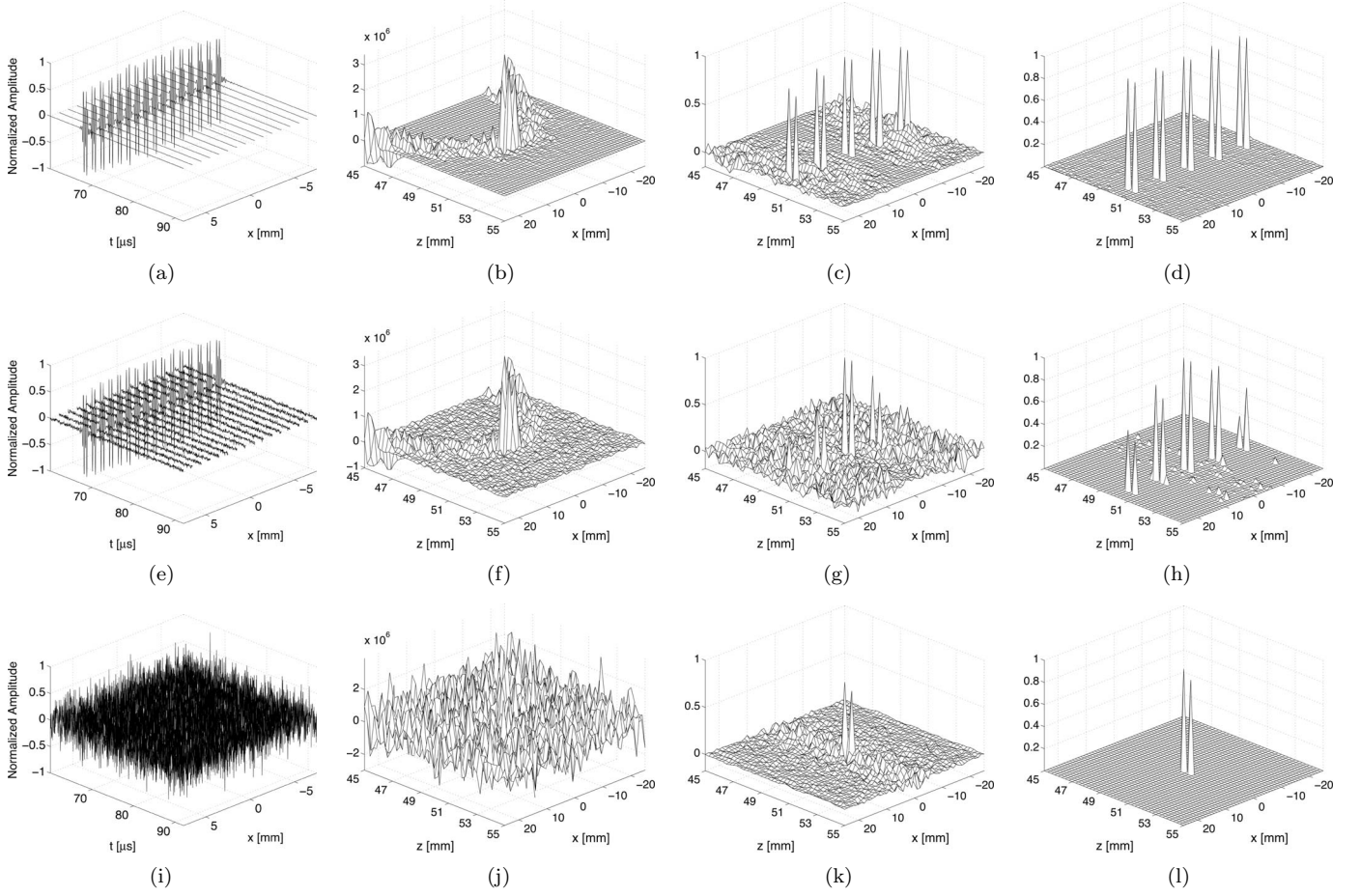
Fig. 7. Simulated data (a), (e), and (i) for five pairs of point targets at $x = -20, -10, 0, 10,$ and 20 mm, at $z = 50$ and $z = 50.5$ mm, respectively, and reconstructions using the DAS (b), (f), and (j), the LMMSE (c), (g), and (k), and the PCQP (d), (h), and (l) algorithms. (a) Data, SNR = 18.0 dB. (b) DAS, SNR = 18.0 dB. (c) LMMSE, SNR = 18.0 dB. (d) PCQP, SNR = 18.0 dB. (e) Data, SNR = 3.4 dB. (f) DAS, SNR = 3.4 dB. (g) LMMSE, SNR = 3.4 dB. (h) PCQP, SNR = 3.4 dB. (i) Data, SNR = −10.1 dB. (j) DAS, SNR = −10.1 dB. (k) LMMSE, SNR = −10.1 dB. (l) PCQP, SNR = −10.1 dB.

$$\hat{\mathbf{o}} = \mathbf{K}_{\text{LMMSE}}\mathbf{y} \approx \mathbf{C}_{\text{o}}\mathbf{P}^T(\mathbf{P}\mathbf{C}_{\text{o}}\mathbf{P}^T)^{-1}\mathbf{y},$$
$$= \mathbf{P}^T(\mathbf{P}\mathbf{P}^T)^{-1}\mathbf{y}, \tag{17}$$

where we have $\mathbf{C}_{\text{o}} = \sigma_{\text{o}}^2\mathbf{I}$; that is, the LMMSE estimator reduces to the least squares (LS) solution [27]. The potential danger with the LS estimate is that the matrix $\mathbf{P}\mathbf{P}^T$ normally has eigenvalues close to zero and the operation $(\mathbf{P}\mathbf{P}^T)^{-1}\mathbf{y}$ will therefore result in a strong noise amplification if there is even the slightest error in $\mathbf{y}$.

The PCQP estimator has a behavior similar to that of the LMMSE estimator. If the noise is large, then the factor $\mathbf{1}^T\mathbf{o}$ will dominate over $(\mathbf{y} - \mathbf{P}\mathbf{o})^T\mathbf{C}_{\text{e}}^{-1}(\mathbf{y} - \mathbf{P}\mathbf{o})$, and (14) reduces to

$$\hat{\mathbf{o}} \approx \arg\min_{\mathbf{o}}\ \lambda_{\text{o}}\mathbf{1}^T\mathbf{o}$$
$$\text{subject to} \qquad o_i \geq 0\ \forall i. \tag{18}$$

The minimum of (18) will be attained when $\hat{\mathbf{o}} = \mathbf{0}$; hence the most likely estimate when the noise goes to infinity is where the prior has its maximum.

From the discussion above, we note that it can be potentially dangerous to use an overly optimistic setting of the

SNR value, and also, an overly pessimistic setting results in reconstruction results similar to the matched filter for the LMMSE estimator. The span where the model-based methods presented here are superior to DAS imaging is, however, rather large.

As a final comment about tuning the SNR parameters in these methods, we note that since $\mathbf{e}$ accounts for more errors than only measurement noise, the SNR setting should in general be lower than the measured noise variance indicates. If the reconstruction performance is poor with this setting, then either (a) the model errors are large and another model should to be considered, or (b) the measurement noise is large, resulting in reconstruction performance similar to that of matched filters, and another design of the experiment should be considered.

To summarize, the general observation from the simulations presented in this section is that it is the spatial distribution of acoustic energy that is most important for the reconstruction performance, not the actual pulse shape. More specifically, the reconstruction performance of the model-based methods employed here mostly depends on the SNR in the particular region and not the length or
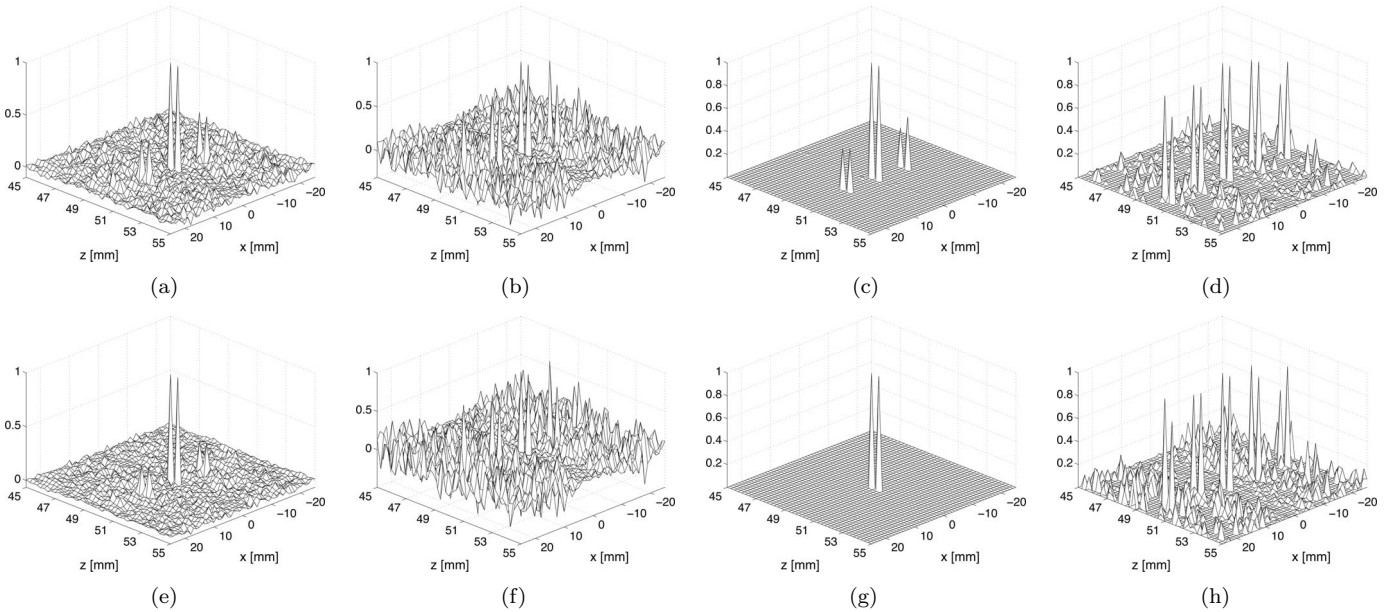
Fig. 8. Reconstructions using the LMMSE and PCQP estimators, for four SNRs that deviate from the true SNR (for five pairs of point targets at $x = -20$, -10, 0, 10, and 20 mm, at $z = 50$ and $z = 50.5$ mm, respectively). The true SNR was 3.4 dB (the LMMSE and the PCQP estimates using the true SNR is shown in Fig. 7(g) and (h), respectively). (a) LMMSE estimate using a 4 times too low SNR. (b) LMMSE estimate using a 4 times too high SNR. (c) PCQP estimate using a 4 times too low SNR. (d) PCQP estimate using a 4 times too high SNR. (e) LMMSE estimate using a 10 times too low SNR. (f) LMMSE estimate using a 10 times too high SNR. (g) PCQP estimate using a 10 times too low SNR. (h) PCQP estimate using a 10 times too high SNR.

shape of the waveform. Moreover, as demonstrated above, the LMMSE and PCQP estimators could estimate targets outside the focusing region, where the transmitted waveforms from each element are not in phase, provided that the SNR is sufficient.

V. Experiments

To verify the presented theoretical results and simulations above, two experiments have been performed. The data have been acquired with an ALLIN array system and a 3-MHz 64-element concave array manufactured by Imasonic (Imasonic S.A., Besançon, France) has been used. The concave Imasonic array, originally designed for inspection of immersed copper and steel specimens, is geometrically focused at 190 mm.[10] The experiments were conducted at room temperature in water using a steel wire target. Since this type of target has a much higher acoustic impedance than water, the requirements for the PCQP method are fulfilled.

We used 16 elements of the array, focused at $z = 50$ mm and steered -20 degrees, and the wire targets were positioned both in the main lobe at $x = -18$ mm and in the grating lobe at $x = 10$ mm, at depth $z = 50$ mm. The reconstruction results are shown in Fig. 9. The results for the DAS method, shown in Fig. 9(a) and (b), demonstrate the typical leakage from the grating lobe associated with conventional beamforming. Also, the tem-

---

[10]For details regarding the data acquisition system and the array, see [28].

poral resolution for the target in the grating lobe is poor. The results for the LMMSE and the PCQP estimators on the other hand, shown in Fig. 9(c)–(f), show that these methods suppressed the grating lobe well for both target positions, and the temporal resolution has also been improved significantly compared to DAS processing.

In summary, both of the model-based LMMSE and PCQP estimators were able to accurately estimate the target strength, regardless whether the wire target was located in the main or the grating lobe. This is in complete agreement with the simulations presented above.

VI. Conclusions

In this paper we have discussed two model-based methods for ultrasonic array imaging; the first one is an optimal linear estimator based on a linear minimum mean squared error (LMMSE) criterion and the second one is a novel nonlinear estimator based on a positivity-constrained quadratic programming (PCQP) problem.

The two model-based methods have been evaluated and their performances have been compared with classical delay-and-sum (DAS) beamforming. It is evident from the results presented here that the two model-based LMMSE and PCQP methods are superior to traditional DAS-based beamforming. In the sense that DAS processing does not perform well for undersampled arrays and when the targets are outside the focusing region, the LMMSE and PCQP methods can reconstruct the targets with high temporal and lateral resolution, provided that the SNR is sufficiently high.
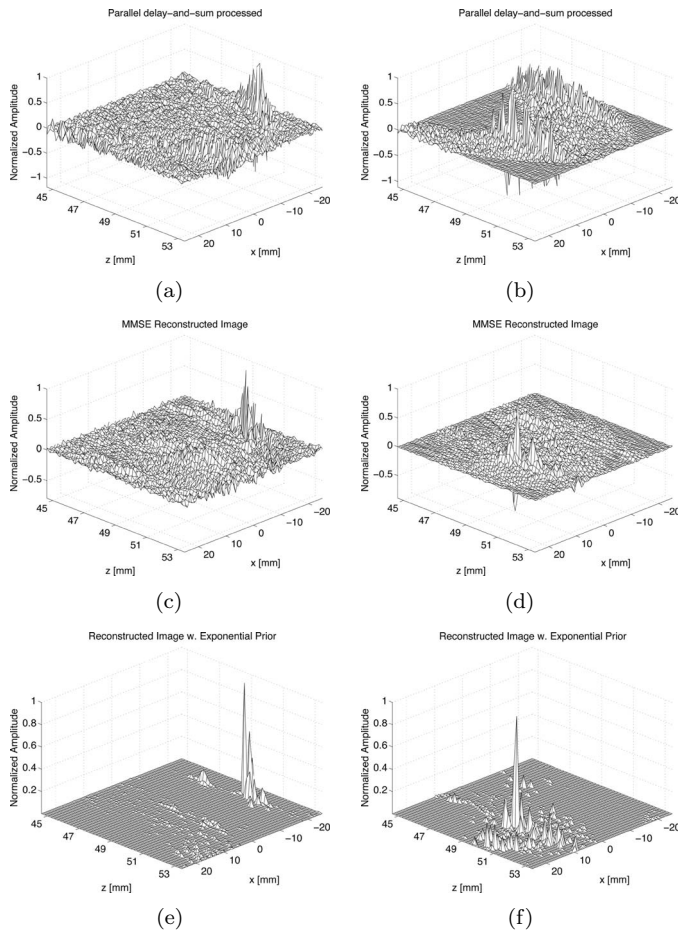
Fig. 9. Reconstructions from measured data using a wire target in the main lobe (a), (c), and (e) and a wire target in the grating lobe (b), (d), and (f). The data were acquired using a 16-element concave Imasonic array. The transmit beam was steered −20 deg and focused at 50 mm. (a) DAS: Target in main lobe. (b) DAS: Target in grating lobe. (c) LMMSE: Target in main lobe. (d) LMMSE: Target in grating lobe. (e) PCQP: Target in main lobe. (f) PCQP: Target in grating lobe.

The general observation from the experiments presented here is that it is the spatial distribution of acoustic energy that is important for the reconstruction performance if the reconstruction method is properly chosen. Also, at least for high-contrast targets, the use of an exponential prior for the scattering amplitudes can give impressive results with very high temporal and lateral resolution. The contrast is also very high and the noise levels in the reconstructions are often very low. The remarkable performance of the PCQP estimator is due to the proper prior information that was incorporated into the reconstruction process, which enables the estimator to effectively discriminate between noise and the target responses.

REFERENCES

[1] M. Tanter, J.-L. Thomas, and M. Fink, "Time reversal and the inverse filter," *J. Acoust. Soc. Amer.*, vol. 108, no. 1, pp. 223–234, July 2000.

[2] O. S. Haddadin and E. S. Ebbini, "Ultrasonic focusing through inhomogeneous media by application of the inverse scattering problem," *J. Acoust. Soc. Amer.*, vol. 104, no. 1, pp. 313–325, July 1998.

[3] R. Stoughton, "Source imaging with minimum mean-squared error," *J. Acoust. Soc. Amer.*, vol. 94, no. 2, pp. 827–834, Aug. 1993.

[4] O. T. von Ramm and S. W. Smith, "Beam steering with linear arrays," *IEEE Trans. Biomed. Eng.*, vol. 30, pp. 438–452, Aug. 1983.

[5] K. E. Thomenious, "Evaluation of ultrasound beamformers," in *Proc. IEEE Ultrason. Symp.*, 1996, p. 1615.

[6] J. A. Seydel, *Ultrasonic Synthetic-Aperture Focusing Techniques in NDT*. ser. Research Techniques for Nondestructive Testing, New York: Academic Press, 1982.

[7] S. R. Doctor, T. E. Hall, and L. D. Reid, "SAFT—The evolution of a signal processing technology for ultrasonic testing," *NDT International*, vol. 19, no. 3, pp. 163–172, June 1986.

[8] M. Karman and M. O'Donnell, "Synthetic aperture imaging for small scale systems," *IEEE Trans. Ultrason., Ferroelect., Freq. Contr.*, vol. 42, no. 3, pp. 429–442, May 1995.

[9] G. S. Kino, *Acoustic Waves: Devices, Imaging and Analog Signal Processing.* Prentice-Hall Signal Processing Series, vol. 6, Englewood Cliffs, NJ: Prentice-Hall, 1987.

[10] J. Shen and E. Ebbini, "A new coded-excitation ultrasonic imaging system—Part I: Basic principles," *IEEE Trans. Ultrason., Ferroelect., Freq. Contr.*, vol. 43, no. 1, pp. 131–140, Jan. 1996.

[11] B. Delannoy, R. Toutguet, C. Bruneel, E. Bridoux, J. M. Rouvaen, and H. Lasota, "Acoustical image reconstruction in parallel-processing analog electronic systems," *J. Appl. Phys.*, vol. 50, no. 5, pp. 3153–3159, May 1979.

[12] D. P. Shattuck, M. D. Weinshenker, S. W. Smith, and O. T. von Ramm, "Explososcan: A parallel processing technique for high speed ultrasound imaging with linear phased arrays," *J. Acoust. Soc. Amer.*, vol. 75, no. 4, pp. 1273–1282, Apr. 1984.

[13] O. T. von Ramm, S. W. Smith, and H. G. Pavy, Jr., "High-speed ultrasound volumetric imaging system. II. Parallel processing and image display," *IEEE Trans. Ultrason., Ferroelect., Freq. Contr.*, vol. 38, no. 2, pp. 109–115, Mar. 1991.

[14] F. Lingvall, T. Olofsson, and T. Stepinski, "Synthetic aperture imaging using sources with finite aperture: Deconvolution of the spatial impulse response," *J. Acoust. Soc. Amer.*, vol. 114, no. 1, pp. 225–234, July 2003.

[15] F. Lingvall, "A method of improving overall resolution in ultrasonic array imaging using spatio-temporal deconvolution," *Ultrasonics*, vol. 42, pp. 961–968, Apr. 2004.

[16] P. R. Stepanishen, "Transient radiation from pistons in an infinite planar baffle," *J. Acoust. Soc. Amer.*, vol. 49, pp. 1629–1638, 1971.

[17] H. Lasota and R. Salamon, "Application of time-space impulse responses to calculations of acoustic field in imaging systems," *Acoust. Imag.*, vol. 10, pp. 493–512, 1980.

[18] A. Lhémery, "Impulse-response method to predict echo-responses from targets of complex geometry. Part I: Theory," *J. Acoust. Soc. Amer.*, vol. 90, no. 5, pp. 2799–2807, Nov. 1991.

[19] R. J. Zemp, C. K. Abbey, and M. F. Insana, "Linear system models for ultrasound imaging: Application to signal statistics," *IEEE Trans. Ultrason., Ferroelect., Freq. Contr.*, vol. 50, no. 6, pp. 642–654, June 2003.

[20] B. Piwakowski and K. Sbai, "A new approach to calculate the field radiated from arbitrarily structured transducer arrays," *IEEE Trans. Ultrason., Ferroelect., Freq. Contr.*, vol. 46, no. 2, pp. 422–440, Mar. 1999.

[21] J. A. Jensen and N. B. Svendsen, "Calculation of pressure fields from arbitrarily shaped, apodized, and excited ultrasonic transducers," *IEEE Trans. Ultrason., Ferroelect., Freq. Contr.*, vol. 39, no. 2, pp. 262–267, Mar. 1992.

[22] F. Lingvall and B. Piwakowski, "The DREAM Toolbox: A freeware MATLAB toolbox for simulating acoustic fields radiated from common ultrasonic transducer types and arbitrarily complicated ultrasonic transducers arrays," available online at: http://www.signal.uu.se/Toolbox/dream/.

[23] E. T. Jaynes, *Probability Theory: The Logic of Science.* 1st ed. Cambridge, UK: Cambridge University Press, 2003.

[24] J. Nocetal and S. J. Wright, *Numerical Optimization.* Berlin: Springer-Verlag, 1999.

[25] G. R. Lockwood, P.-C. Li, M. O'Donnell, and F. S. Foster, "Optimizing the radiation pattern of sparse periodic linear arrays," *IEEE Trans. Ultrason., Ferroelect., Freq. Contr.*, vol. 43, pp. 7–14, Jan. 1997.

[26] A. Austeng, S. Holm, P. Weber, N. Aakvaag, and K. Iranpour, "1D and 2D algorithmically optimized sparse arrays," in *Proc. IEEE Ultrason. Symp.*, 1997, pp. 1683–1686.

[27] S. M. Kay, *Fundamentals of Statistical Signal Processing: Estimation Theory.* vol. I, New York: Prentice-Hall, 1993.

[28] P. Wu and T. Stepinski, "Spatial impulse response method for predicting pulse-echo fields from linear array with cylindrically concave surface," *IEEE Trans. Ultrason., Ferroelect., Freq. Contr.*, vol. 46, no. 5, pp. 1283–1297, Sep. 1999.

Tomas Olofsson was born 1968 in Sandviken, Sweden. He received his M.Sc. degree in engineering physics in 1994 and the Ph.D. degree in signal processing in 2000, both from Uppsala University. He is currently working as an associate professor at the Signals and Systems group, Uppsala University, Sweden. His research concerns inference problems, in particular, inverse problems in ultrasonics.

Fredrik Lingvall was born 1967 in Uppsala, Sweden. He received a university diploma in electrical engineering in 1992, a M.Sc. degree in engineering physics in 1997, a Licentiate degree in 2002, and the Ph.D. degree in electrical engineering with specialization in signal processing in 2004, all from Uppsala University, Sweden. He is currently working as a researcher at the group for Digital Signal Processing and Image Analysis, Department of Informatics, University of Oslo, Norway. His research concerns inference problems in acoustic imaging.